Structural and molecular modelling studies reveal a new mechanism of action of chloroquine and hydroxychloroquine against SARS-CoV-2 infection

Coralie Di Scala, Jacques Fantini, Henri Chahinian, Nouara Yahi

Synergistic antiviral effect of hydroxychloroquine and azithromycin in combination against SARS-CoV-2 : what molecular dynamics studies of virus-host interactions reveal

Jacques Fantini, Henri Chahinian and Nouara Yahi

[1]INSERM UMR_S 1072, 13015 Marseille, France ; Aix-Marseille Université, 13015 Marseille, France.

Int J Antimicrob Agents 2020 Aug;56(2):106020.

doi: 10.1016/j.ijantimicag.2020.106020. Epub 2020 May 13.

Abstract

The emergence of SARS-coronavirus-2 (SARS-CoV-2) is responsible for a global pandemic disease referred to as coronavirus disease 19 (Covid-19). Hydroxychloroquine/azithromycin combination therapy is currently tested for curing Covid-19, with promising results. However, the molecular mechanism of action of this combination is not established yet. Using molecular dynamics (MD) simulations we show that both drugs act in synergy to prevent any close contact between the virus and the plasma membrane of host cells. We reveal unexpected molecular similarity between azithromycin and the sugar moiety of GM1, a lipid raft ganglioside acting as a host attachment cofactor for respiratory viruses. Due to this mimicry, azithromycin interacts with the ganglioside-binding domain of SARS-CoV-2 spike protein. This binding site shared by azithromycin and GM1 displays a conserved amino acid triad Q-134/F-135/N-137 located at the tip of the spike protein. We also show that hydroxychloroquine molecules can saturate virus attachment sites on gangliosides in the vicinity of the primary coronavirus receptor ACE-2. Taken together, these data show that azithromycin is directed against the virus, whereas hydroxychloroquine is directed against cellular attachment cofactors. We conclude that both drugs act as competitive inhibitors of SARS-CoV-2 attachment to the host cell membrane. This is consistent with a synergistic antiviral mechanism at the plasma membrane level, where the most efficient therapeutic intervention probably stands. This molecular mechanism may explain the beneficial effects of hydroxychloroquine/azithromycin combination therapy in patients with Covid-19. Incidentally, our data suggest that the conserved Q-134/F-135/N-137 triad could be considered as a target for vaccine strategies.

Keywords: coronavirus, pandemic, SARS-CoV-2, ganglioside, azithromycin, chloroquine

Abbreviations: ACE-2, angiotensin converting enzyme-2; CLQ, chloroquine; CLQ-OH, hydroxychloroquine; COVID-19, coronavirus disease 19; NTD, N-terminal domain; RBD, receptor binding domain; SARS-CoV, severe acute respiratory syndrome coronavirus; SARS-CoV-2, SARS-coronavirus-2

Funding: This research did not receive any specific grant from funding agencies in the public, commercial, or not-for-profit sectors.

1. Introduction

The emergence of the novel pathogenic SARS-coronavirus 2 (SARS-CoV-2) is responsible for a global pandemic disease referred to as coronavirus disease 19 (Covid-19) [1]. In face of the health emergency, it is of critical urgency to find a cure for stopping the pandemic. Among the potential solutions currently under investigation, a combination bitherapy consisting of the anti-malarial drug hydroxychloroquine with antibiotic azithromycin has received special attention. Following initial reports from China indicating a potential effect of chloroquine (CLQ) [2], a preliminary clinical trial was implemented in France on a small cohort of COVID-19 patients [3]. A significant viral load reduction was observed in the 20 patients treated with hydroxychloroquine (CLQ-OH) [3], a CLQ derivative with increased solubility in water and decreased toxicity [4]. With the aim of preventing bacterial super-infection, six additional patients of this trial also received azithromycin (ATM) for five days. All these patients had undetectable viral load after 6 days [3]. Thus, although these promising data need clinical confirmation with more patients, CLQ-OH/ATM combination therapy already appears superior to CLQ alone as a first line-treatment for COVID-19.

Both CLQ-OH and ATM are repositioned drugs and their antiviral mechanism of action, especially in combination, remains mostly unclear. In vitro studies have shown that CLQ-OH inhibits SARS-CoV-2 [4-6]. Far less is known about the antiviral effects of ATM, which has been suggested to interfere with influenza virus internalization [7]. Interestingly, CLQ is also considered as an inhibitor of endocytic pathways through an elevation of endosomal pH [8]. However, several reports indicate that CLQ could also prevent virus attachment through a direct effect on host cell surface molecules [9,10].

The very first step of human coronaviruses replication cycle is the attachment to the plasma membrane of target cells, which is mediated by a membrane protein receptor, i.e. angiotensin converting enzyme-2 (ACE-2) in the case of SARS-CoV-2 [11]. Moreover, coronaviruses are also dependent upon sialylated membrane components such as gangliosides that act as attachment cofactors within lipid raft membrane platforms [12-14]. As ACE-2 is localized in lipid rafts [15], SARS-CoV-2 infection requires specific targeting to these plasma membrane microdomains, where multivalent interactions between the spike protein and raft components can take place. In line with notion, lipid raft disruption through cholesterol depletion resulted in a significant reduction of human coronavirus SARS-CoV infection [15]. The recent identification of a potential ganglioside-binding domain in the N-terminal domain (NTD) of the SARS-CoV-2 spike protein, and its potential role in membrane recognition [10], prompted us to study the molecular relationship between this domain, gangliosides, ATM and CLQ-OH. To this end, we used our molecular modeling strategy that has been successfully applied for unraveling the molecular mechanisms of protein binding to raft lipid components including gangliosides [16,17] and cholesterol [18,19].

2. Materials and Methods

2.1.Pdb files

The SARS-CoV-2 spike protein trimer in the prefusion conformation was obtained from pdb file # 6VSB [20]. Hydroxychloroquine (CLQ-OH) is (RS)-2-[{4-[(7-chloroquinolin-4-yl)amino]pentyl}(ethyl)amino]ethanol. CLQ-OH was generated by hydroxylation of chloroquine (CLQ) and validated as previously described [10]. CLQ was retrieved from pdb file # 4V2O (CLQ co-crystallized with saposin B) [21].

Azithromycin (ATM) is (2R,3S,4R,5R,8R,10R,11R,12S,13S,14R)-11-[(2S,3R,4S,6R)-4-(dimethylamino)-3-hydroxy-6-methyloxan-2-yl]oxy-2-ethyl-3,4,10-trihydroxy-13-[(2R,4R,5S,6S)-5-hydroxy-4-methoxy-4,6-dimethyloxan-2-yl]oxy-3,5,6,8,10,12,14-heptamethyl-1-oxa-6-azacyclopentadecan-15-one. The 3D structure of ATM was obtained from pdb file # 5UXD (ATM co-crystallized with macrolide 2'-phosphotransferase) [22].

2.2. Molecular modelling and visualization tools

Molecular modelling studies were performed using Hyperchem (http://www.hyper.com), Deep View/Swiss-Pdb viewer (https://spdbv.vital-it.ch) and Molegro Molecular viewer (http://molexus.io/molegro-molecular-viewer) as described previously [16-19,23]. Lennard-Jones parameters and atomic charges of ATM obtained from pdb file # 5UXD were checked with Hyperchem. The molecular modelling protocol consisted of docking, equilibration, and subsequent 50-ns MD simulations with CHARMM force field [16,24] in Hyperchem. The starting point for ATM docking was done by manual positioning on the NTD and RBD surfaces of SARS-CoV-2 spike protein (chain A) with full consideration of the drug's properties. In addition, a series of 20 randomly positioned ATM molecules covering the whole NTD surface were also analyzed. Energy minimization of each system was then performed with the Polak-Ribière conjugate gradient algorithm, with CHARMM force field in Hyperchem, using a maximum of 3×10^5 steps, and a root-mean-square (RMS) gradient of 0.01 kcal. $Å^{-1}.mol^{-1}$ as the convergence condition. According to the validation ligand-binding protocol [25], the optimized docked structures were used as the initial structures for MD simulations with the following parameters: heat time 5 ps, run time, 10 ps, step size 1 fs, starting temperature 0 K, simulation temperature 300 K, temperature step 30 K, bath relaxation time step size 0.1 ps. Each complex was submitted to 50-ns long MD trajectories,

replicated three times, with convergent trajectories obtained. Frames were saved at 10 ns intervals for subsequent analysis. The final complex obtained with chain A was reintroduced in the trimeric spike structure (pdb file # 6VSB) with Molegro Molecular viewer and with Deep View Swiss-Pdb viewer. Similar results were obtained with both programs. The energies of interaction were extracted from the Ligand Energy Inspector function of Molegro Molecular viewer. Molecular volumes were calculated by the QSAR function of Hyperchem.

2.3. Ganglioside GM1

The initial coordinates of ganglioside GM1 were obtained from CHARMM-GUI Glycolipid Modeler [24] (http://www.charmmgui.org/?doc=input/glycolipid;) which uses the internal coordinate information of common glycosidic torsion angle values, orients the ganglioside perpendicular to the membrane, and performs Langevin dynamics with a cylindrical restraint potential to keep the whole GM1 molecule cylindrical, especially the membrane-embedded ceramide part. In the next step, we included the saccharide part of the ganglioside in a periodic box solvated with 1128 water molecules (dimensions: 34848 $Å^3$ with x = 33 Å, y = 32 Å, z = 33 Å). The system was energy-minimized 6 times switching alternatively between runs using steepest descent gradients or Polak-Ribière conjugate gradients until convergence to machine precision [16]. The dimer of ganglioside GM1 interacting with 4 CLQ-OH molecules was obtained by MD simulations of a previously described model [10]. To mimic GM1 gangliosides in a typical lipid raft membrane domain, two GM1 molecules were merged with eight cholesterol and two sphingomyelin lipids. The whole system was optimized, merged with SARS-CoV-2 spike protein (chain A) and submitted to MD simulations with the same conditions as those used for the ATM-spike protein complex (50-ns run in triplicate). For comparison, similar MD simulations

were performed on an isolated GM1 dimer in the CHARMM-GUI membrane-compatible topology but without surrounding lipids.

3. Results

3.1. Molecular mimicry between ATM and ganglioside GM1

The chemical structure of ATM is shown in Figure 1a. The molecule contains two sugar-like pyranyl rings, one with nitrogen-containing group (N-pyr), the other with an acetyl group (Ac-pyr). The remaining part of the molecule is cyclic, so that its overall conformational flexibility, although significant, is restricted to a limited spatial volume of 2082 $Å^3$ (Figure 1b). Interestingly, this volume is almost the same as the one of the saccharide part of ganglioside GM1 (2293 $Å^3$, Figure 1b), a lipid raft ganglioside that plays a critical role in the binding and endocytosis of respiratory viruses [26], including pathogenic human coronaviruses [27]. Beyond their similar spatial volume, the saccharide part of GM1 and ATM also share some analogous chemical features including sugar rings and a solvent-accessible surface dotted with several CH and OH groups (Figure 1b). This molecular similarity is further illustrated in Figure S1 where ATM is superimposed on the saccharide part of GM1.

Given that the SARS-CoV-2 spike protein displays a ganglioside-binding site at the tip of its NTD [10], we considered the possibility that ATM, as a "ganglioside mimic", could also bind to this site. The structural features of the SARS-CoV-2 spike in the prefusion conformation [20] are shown in Figure 1c. It consists of three interdigitated spike proteins that provide the virus its typical corona like shape in electron microscopy images. In each subunit, the most distant part from the viral envelope is divided in two separate domains, the NTD and the receptor-binding domain (RBD). The NTD has a flat surface available for ganglioside binding [10], and this process is independent from the ACE-2 receptor recognition which occurs at the tip of the RBD [11,20]. When seen from above, the viral

spike has a typical triangle shape, with a ganglioside-binding domain at each apex. Thus, the spike central area is devoted to ACE-2 binding, leaving three peripheric flat surface areas available for ganglioside attachment. Such dual ganglioside/receptor binding is commonly used by pathogenic viruses such as HIV-1 [28-30] and bacterial neurotoxins [16]. By combining the high affinity for a single protein receptor with multiple low affinity attachment sites, these pathogens have selected a very efficient pathway to gain entry into host cells.

3.2. Characterization of an ATM binding site at the tip of SARS-CoV-2 spike protein

When ATM molecules were merged with the SARS-CoV-2 spike protein, a very good fit was evidenced for one particular pose at the tip of protein (Figure 2). All other docking attempts on the NTD or the RBD of the spike protein were unsuccessful (Figure S2) as they did not satisfy the minimum cutoff values. Not surprisingly, their trajectories started destabilizing before 10 ns. In contrast, ATM #1 (colored in yellow in Figure S2) remained bound to the spike protein throughout the simulation process (Figure 3). It is interesting to note that a significant movement of the drug was observed from its docked pose to stable MD pose (dock-to-MD transition), especially during the first 10-ns of simulations (Figure S3). A stable complex association was then reached after 10 ns. We noticed that three amino acid residues, referred to as the "QFN triad", exhibited significant conformational rearrangement during the binding process: Q-134, F-135 and N-137 (Figure 3). The principal moves consisted in a significant reorientation of the aromatic ring of F-135, from suboptimal stacking to stabilized T-shape CH-π interaction, and a concomitant retraction of the Q-134 side chain. Fluctuations during the 10-50 ns period did not affect the overall geometry of the complex, which converged to a mean energy of interaction of 92.4 ± 5.8

kJ.mol^{-1} as determined from triplicate MD simulations (Table S1). Schematically, the binding site is formed by two discontinuous regions of the protein, including the QFN triad with additional C-136, D-138, R-158 and S-161 residues (Figures 4 and 5). These seven amino acid residues accounted for almost 90% of the whole energy of interaction (Table S1 and Figure 5).

The complex was stabilized by hydrogen bonds, CH-π and van der Waals interactions distributed over the whole ATM molecule (Figure 4).

3.3. SARS-CoV-2 spike protein interactions with gangliosides in a lipid raft domain

Based on recent in-silico data that led to the characterization of ganglioside-spike protein interactions [10], we performed MD simulations with GM1 gangliosides surrounded by typical raft lipids, i.e. sphingomyelin and cholesterol (Figures 5 and 6). These new data confirmed and extended our previous results obtained with isolated gangliosides [10]. Indeed, cholesterol and sphingomyelin appeared to stabilize the typical chalice-shaped GM1 dimer which serves as a landing platform for SARS-CoV-2 spike protein (Figure 6). Moreover, the histograms of Figure 5 show that all amino acid residues of the spike protein that are involved in ATM binding, including the QFN triad, are also essential for GM1 binding in the lipid raft environment (Table S1 and Figure 5). Taken together, these data suggest that the NTD of the viral glycoprotein may indeed display a common ganglioside/ATM binding site, in agreement with our working hypothesis. Sequence alignments revealed that this common binding site, including the QFN triad, is totally conserved among clinical isolates of SARS-CoV-2 from various geographic origins worldwide (Figure 7). It is also conserved in bat RaTG13, which further illustrates the close relationship between this bat coronavirus and the SARS-CoV-2 strains that are currently circulating around the world. We thus suggest considering this region of the NTD for SARS-CoV-2 vaccine strategies. However, the motif has a different sequence signature in

other animal- and human-related SARS coronaviruses (Figure 7), suggesting a recent evolution which may be linked to the higher contagiousness of SARS-CoV-2 compared with other human coronaviruses.

3.4. Synergistic antiviral effects of ATM and CLQ-OH

Overall, these molecular modelling studies are consistent with the notion that ATM might inhibit SARS-CoV-2 infection through direct binding to virus spike and subsequent neutralization of the infection process which requires spike protein recognition and attachment to gangliosides. This mechanism of action is illustrated in Figure 8. By comparing the models in Figure 8a and 8b, one can see that both ATM and gangliosides bind to the same site of the spike protein, centered on the QFN triad. Thus, in presence of ATM, the virus spike would be unable to reach gangliosides on the host plasma membrane (Figure 8c). To the best of our knowledge, it is the first time that such a mechanism of action is proposed for explaining the antiviral effect of ATM.

Then we looked at CLQ-OH and its interaction with GM1. We recently published a model describing a complex formed by one GM1 and two CLQ-OH molecules [10]. For the sake of comparison, we applied to this model the same molecular modelling approaches as for ATM (i.e. in presence of surrounding raft lipids). We obtained a stable complex formed by a ganglioside dimer, each monomer being associated with two CLQ-OH molecules (Figure 8d). The stability of this complex is reinforced by a rearrangement of CLQ-OH molecules which, while interacting with the saccharide part of GM1, also interact with each other. Consequently, the surface of the ganglioside is almost completely masked, so that the ganglioside dimer can no longer be recognized by the viral spike (Figure 8c). In presence of both ATM and CLQ-OH, virus-ganglioside interactions are efficiently blocked, preventing any close contact between the virus and the plasma membrane of host cells. The molecular details of this synergistic antiviral effect are worth mentioning. As shown in

Figures 5 and 8e and Table S1, the QFN triad of the virus spike protein is predicted to interact with the central region of the ganglioside dimer. If we metaphorically compare the dimer to a butterfly, this region corresponds to the insect's head between the wings. For its part, CLQ-OH binds to the wings (Figure 8d), whereas ATM neutralizes the QFN triad of the virus spike protein (Figure 8f). Indeed, all attempts to obtain a stable raft-spike protein complex aborted when GM1 was covered by CLMQ-OH and when ATM was bound to the spike protein. In the particular case of ATM, these data confirm that the QFN triad is critical for GM1 recognition and that although other residues are involved (Figure 5 and Table S1), the whole binding process is fully controlled by the primary interaction driven by the QFN triad. In agreement with this notion, mutating the QFN triad with alanine residues resulted in aborted ATM binding process at the post-docking steps. Taken together, our molecular modelling studies suggest that CLQ-OH and ATM, when bound to their respective targets, totally mask the complementary surfaces provided by the lipid raft and the virus spike (Figure 8c): CLQ-OH binds to GM1 and covers the wing, ATM binds to the virus spike and prevents any interaction with the center area of the ganglioside dimer. Hence both drugs act as competitive inhibitors of SARS-CoV-2 attachment to the host cell membrane.

4. Discussion

In this study, we used molecular modelling approaches specifically dedicated to virus-host interactions to unravel the antiviral mechanism of action of ATM and CLQ-OH in combination. Our method included a first round of molecular docking, followed by MD simulations of protein-ligand interactions to assess the robustness of each model [25]. Such computer-assisted simulations are particularly helpful for studying protein-ganglioside interactions since crystallographic approaches are usually limited to the water-soluble saccharide part of the ganglioside, neglecting their membrane embedded ceramide part [31]. Unfortunately, the ceramide moiety of gangliosides has a marked effect on the

saccharide part with which it interacts, resulting in significant restriction of its conformational possibilities [32]. Therefore, data obtained with oligosaccharides cannot be systematically transposed to intact gangliosides. Molecular modelling approaches allowed us to get around this difficulty by studying whole gangliosides in membrane-compatible conformations [16,32,33]. The MD simulations performed in the present study were done on gangliosides surrounded by cholesterol and sphingomyelin, which mimic a lipid raft environment.

To date, there are several structural data of the SARS-CoV-2 protein in the prefusion conformation or bound to its primary receptor ACE-2 [11, 20]. However, ACE-2 is in lipid rafts and raft disruption induces a marked decrease of virus infection [15]. Thus, it is likely that the virus interacts with the raft surface through multivalent contacts involving both ACE-2 and gangliosides. The fact that the RBD and the ganglioside-binding domain belong to distinct parts of the trimeric spike is consistent with this notion. Such a complex network of virus-host cell membrane interactions is consistent with previously characterized virus infection strategies. Indeed, the HIV-1 fusion process driven by gp120 and gp41 envelope proteins involves a receptor (CD4), a coreceptor (chiefly CCR5) and glycosphingolipid cofactors [39]. Like SARS-CoV-2, the pentameric capsid protein of SV40, and polyoma viruses display three distinct binding sites for gangliosides, which serve as critical receptors for these non-enveloped viruses in lipid raft domains [40].

Our MD simulations suggest that both CLQ-OH and ATM may block SARS-CoV2 binding to gangliosides via mirror competitive mechanisms. ATM, which has some molecular similarity with GM1 sugar, can thus occupy the ganglioside-binding domain of the spike protein and neutralize virus binding to lipid rafts. CLQ-OH covers the ganglioside surface, and thus also prevents virus-membrane interaction through a complementary mechanism. Each of these drugs might be efficient alone to block virus attachment, ATM through virus

binding, CLQ-OH through ganglioside binding. Since both drugs interfere with the same mechanism but with distinct molecular targets, they are expected to work together in synergy, as suggested by recent clinical data [3].

The posology of the combination therapy for Covid-19 is 600 mg CLQ-OH and 250 mg ATM per day [3,34]. This ratio corresponds to a molar ratio of five CLQ-OH for one ATM. Our in silico calculations indicate a binding ratio of four CLQ-OH for one ATM, which is close to the posology. Furthermore, since ATM shares structural similarity with the saccharide part of GM1, one should ask whether ATM could bind to CLQ-OH and by this way reduce the potential effectiveness of this combination therapy. However, since ATM and CLQ-OH have been reported to synergistically decrease SARS-CoV-2 load in infected patients [3], drug cross-neutralization is very unlikely. Consistently, we could not evidence any stable ATM-CLQ-OH complexes by our molecular modelling approaches.

In any case, the molecular mimicry between ATM and the saccharide part of GM1 gives new perspectives on the therapeutic effect of this macrolide antibiotic which warrants further exploration. Moreover, the fact that ganglioside GM1 is a molecular target for CLQ-OH might explain the indication of this drug in rheumatologic disorders such as lupus and rheumatoid arthritis [35,36]. Indeed, GM1 overexpression and anti-GM1 antibodies are a hallmark of these diseases [37,38]. Thus, our data incidentally suggest that the therapeutic effect of CLQ-OH in these cases could also be related to its ganglioside-binding properties.

5. Conclusion

We conclude that ATM and CLQ-OH have synergistic antiviral effect on SARS-CoV-2 infection, which supports the use of this combination therapy for the Covid-19 pandemic. In this bitherapy, one molecule (ATM) is directed against the virus, while the second one (CLQ-OH) is directed against cellular attachment cofactors. Yet both drugs are predicted

to act in synergy to prevent the very first step of SARS-CoV-2 infection, at the plasma membrane level, where the most efficient therapeutic intervention probably stands. The conserved QFN triad of the SARS-CoV-2 spike protein, which is recognized by both gangliosides and ATM, should be considered as a target for neutralizing antibodies in vaccine strategies. Our molecular modeling approaches, based on the search for ganglioside saccharide mimicry, might be useful to identify other ATM binding sites on virus proteins, and more generally to predict the efficacy of any potential repurposed and/or innovative drug candidates before clinical evaluation. In this respect, we suggest testing the antiviral association of ATM with short synthetic peptides specifically designed to target gangliosides without toxicity [17,33].

6. References

1. Wu F, Zhao S, Yu B, Chen YM, Wang W, Song ZG, Hu Y, Tao ZW, Tian JH, Pei YY, Yuan ML, Zhang YL, Dai FH, Liu Y, Wang QM, Zheng JJ, Xu L, Holmes EC, Zhang YZ. A new coronavirus associated with human respiratory disease in China. Nature 2020; 579: 265-269. DOI: 10.1038/s41586-020-2008-3

2. Gao J, Tian Z, Yang X. Breakthrough: Chloroquine phosphate has shown apparent efficacy in treatment of COVID-19 associated pneumonia in clinical studies. Biosci Trends 2020; 14: 72-73. DOI: 10.5582/bst.2020.01047

3. Gautret P, Lagier JC, Parola P, Hoang VT, Meddeb L, Mailhe M, Doudier B, Courjon J, Giordanengo V, Vieira VE, Dupont HT, Honoré S, Colson P, Chabrière E, La Scola B, Rolain JM, Brouqui P, Raoult D. Hydroxychloroquine and azithromycin as a treatment of COVID-19: results of an open-label non-randomized clinical trial. Int J Antimicrob Agents 2020; 20:105949. DOI: 10.1016/j.ijantimicag.2020.105949

4. Liu J, Cao R, Xu M, Wang X, Zhang H, Hu H, Li Y, Hu Z, Zhong W, Wang M. Hydroxychloroquine, a less toxic derivative of chloroquine, is effective in inhibiting SARS-CoV-2 infection in vitro. Cell Discov 2020; 6:16. DOI: 10.1038/s41421-020-0156-0

5. Yao X, Ye F, Zhang M, Cui C, Huang B, Niu P, Liu X, Zhao L, Dong E, Song C, Zhan S5, Lu R, Li H, Tan W, Liu D. In Vitro Antiviral Activity and Projection of Optimized Dosing Design of Hydroxychloroquine for the Treatment of Severe Acute Respiratory Syndrome Coronavirus 2 (SARS-CoV-2). Clin Infect Dis 2020; pii:ciaa237. DOI: 10.1093/cid/ciaa237

6. Wang M, Cao R, Zhang L, Yang X, Liu J, Xu M, Shi Z, Hu Z, Zhong W, Xiao G. Remdesivir and chloroquine effectively inhibit the recently emerged novel coronavirus (2019-nCoV) in vitro. Cell Res 2020; 30:269–271. DOI: 10.1038/s41422-020-0282-0

7. Tran DH, Sugamata R, Hirose T, Suzuki S, Noguchi Y, Sugawara A, Ito F, Yamamoto T2, Kawachi S, Akagawa KS, Ōmura S, Sunazuka T, Ito N, Mimaki M, Suzuki K. Azithromycin, a 15-membered macrolide antibiotic, inhibits influenza A(H1N1)pdm09 virus infection by interfering with virus internalization process. J. Antibiot. (Tokyo) 2019; 72:759-768. DOI: 10.1038/s41429-019-0204-x

8. Mauthe M, Orhon I, Rocchi C, Zhou X, Luhr M, Hijlkema KJ, Coppes RP, Engedal N, Mari M, Reggiori F. Chloroquine inhibits autophagic flux by decreasing autophagosome-lysosome fusion. Autophagy 2018; 14:1435-1455. DOI: 10.1080/15548627.2018.1474314

9. Vincent MJ, Bergeron E, Benjannet S, Erickson BR, Rollin PE, Ksiazek TG, Seidah NG, Nichol ST. Chloroquine is a potent inhibitor of SARS coronavirus infection and spread. Virol J 2005; 2 : 69. DOI: 10.1186/1743-422X-2-69

10. J. Fantini, C. Di Scala, H. Chahinian, N. Yahi. Structural and molecular modeling studies reveal a new mechanism of action of chloroquine and hydroxychloroquine against SARS-CoV-2 infection. Int J Antimicrob Agents 2020; Apr 3:105960. DOI: 10.1016/j.ijantimicag.2020.105960

11. Yan R, Zhang Y, Li Y, Xia L, Guo Y, Zhou Q. Structural basis for the recognition of the SARS-CoV-2 by full-length human ACE2. Science 2020; 367: 1444-1448. DOI: 10.1126/science.abb2762

12. Matrosovich M, Herrler G,Klenk HD. Sialic Acid Receptors of Viruses. Top Curr Chem 2015; 367:1-28. DOI: 10.1007/128_2013_466

13. Li W, Hulswit RJG, Widjaja I, Raj VS, McBride R, Peng W, Widagdo W, Tortorici MA, van Dieren B, Lang Y, van Lent JWM, Paulson JC, de Haan CAM, de Groot RJ, van Kuppeveld FJM, Haagmans BL, Bosch BJ. Identification of sialic acid-binding function for the Middle East respiratory syndrome coronavirus spike glycoprotein. Proc Natl Acad Sci USA 2017; 114:E8508-E8517. DOI: 10.1073/pnas.1712592114

14. Park YJ, Walls AC, Wang Z, Sauer MM, Li W, Tortorici MA, Bosch BJ, DiMaio, Veesler D. Structures of MERS-CoV spike glycoprotein in complex with sialoside attachment receptors. Nat Struct Mol Biol 2019; 26:1151-1157. DOI: 10.1038/s41594-019-0334-7

15. Glende J, Schwegmann-Wessels C, Al-Falah M, Pfefferle S, Qu X, Deng H, Drosten C, Naim HY, Herrler G. Importance of cholesterol-rich membrane microdomains in the interaction of the S protein of SARS-coronavirus with the cellular receptor angiotensin-converting enzyme 2. Virology 2008; 381:215-221. DOI: 10.1016/j.virol.2008.08.026

16. Flores A, Ramirez-Franco J, Desplantes R1, Debreux K, Ferracci G, Wernert F, Blanchard MP, Maulet Y, Youssouf F, Sangiardi M, Iborra C, Popoff MR, Seagar M, Fantini J, Lévêque C, El Far O. Gangliosides interact with synaptotagmin to form the high-affinity receptor complex for botulinum neurotoxin B. Proc Natl Acad Sci USA 2019; 116: 18098-18108. DOI: 10.1073/pnas.1908051116

17. Yahi N, Fantini J. Deciphering the glycolipid code of Alzheimer's and Parkinson's amyloid proteins allowed the creation of a universal ganglioside-binding peptide. PLoS One 2014; 9:e104751. DOI: 10.1371/journal.pone.0104751

18. Fantini J, Di Scala C, Evans LS, Williamson PT, Barrantes FJ. A mirror code for protein-cholesterol interactions in the two leaflets of biological membranes. Sci Rep 2016; 6:21907. DOI: 10.1038/srep21907

19. Fantini J, D. Carlus D, Yahi N. The fusogenic tilted peptide (67-78) of α-synuclein is a cholesterol binding domain. Biochim Biophys Acta 2011; 1808:2343-2351. DOI: 10.1016/j.bbamem.2011.06.017

20. Wrapp, Wang N, Corbett KS, Goldsmith JA, Hsieh CL, Abiona O, Graham BS, McLellan JS. Cryo-EM structure of the 2019-nCoV spike in the prefusion conformation. Science 2020; 367:1260-1263. DOI: 10.1126/science.abb2507

21. Huta BP, Mehlenbacher MR, Nie Y, Lai X, Zubieta C, Bou-Abdallah F, Doyle RP. The lysosomal protein saposin B binds chloroquine. ChemMedChem 2016 ; 11:277-282 (2016). DOI: 10.1002/cmdc.201500494

22. Pawlowski AC, Stogios PJ, Koteva K, Skarina T, Evdokimova E, Savchenko A, Wright GD. The evolution of substrate discrimination in macrolide antibiotic resistance enzymes. Nat Commun 2018; 9:112-112. DOI: 10.1038/s41467-017-02680-0

23. Di Scala C, Fantini J. Hybrid in silico/in vitro approaches for the identification of functional cholesterol-binding domains in membrane proteins. Methods Mol Biol 2017; 1583:7-19. DOI: 10.1007/978-1-4939-6875-6_2

24. Lee J, Patel DS, Ståhle J, Park SJ, Kern NR, Kim S, Lee J, Cheng X, Valvano MA, Holst O, Knirel YA, Qi Y, Jo S, Klauda JB, Widmalm G, Im W. CHARMM-GUI Membrane Builder for Complex Biological Membrane Simulations with Glycolipids and Lipoglycans. J Chem Theory Comput 2019; 15: 775-786. DOI: 10.1021/acs.jctc.8b01066

25. Hollingsworth SA, Dror RO. Molecular Dynamics Simulation for All. Neuron 2018; 99:1129-1143. DOI: 10.1016/j.neuron.2018.08.011

26. Verma DK, Gupta D, Lal SK. Host Lipid Rafts Play a Major Role in Binding and Endocytosis of Influenza A Virus. Viruses 2018; pii: E650. DOI: 10.3390/v10110650

27. Lu Y, Liu DX, Tam JP. Lipid rafts are involved in SARS-CoV entry into Vero E6 cells. Biochem Biophys Res Commun 2008; 369:344-349. DOI: 10.1016/j.bbrc.2008.02.023

28. Fantini J, Yahi N. Brain Lipids in Synaptic Function and Neurological Disease. Clues to Innovative Therapeutic Strategies for Brain Disorders. Elsevier Academic Press; San Francisco: 2015. ISBN: 9780128001110.

29. Hammache D, Piéroni G, Yahi N, Delézay O, Koch N, Lafont H, Tamalet C, Fantini J. Specific interaction of HIV-1 and HIV-2 surface envelope glycoproteins with

monolayers of galactosylceramide and ganglioside GM3. J Biol Chem 1998; 14:7967-7971. DOI: 10.1074/jbc.273.14.7967

30. Fantini J, Garmy N, Mahfoud R, Yahi N. Lipid rafts: structure, function and role in HIV, Alzheimer's and prion diseases. Expert Rev Mol Med 2002; 4: 1-22. DOI: 10.1017/S1462399402005392

31. Berntsson RP, Peng L, Dong M, Stenmark P. Structure of dual receptor binding to botulinum neurotoxin B. Nat Commun 2013; 4: 2058. DOI: 10.1038/ncomms3058

32. Fantini J, Yahi N, Garmy N. Cholesterol accelerates the binding of Alzheimer's β-amyloid peptide to ganglioside GM1 through a universal hydrogen-bond-dependent sterol tuning of glycolipid conformation. Front Physiol 2013; 4:120. DOI: 10.3389/fphys.2013.00120

33. Di Scala C, Yahi N, Boutemeur S, Flores A, Rodriguez L, Chahinian H, Fantini J. Common molecular mechanism of amyloid pore formation by Alzheimer's β-amyloid peptide and α-synuclein. Sci Rep 2016; 6:28781. DOI: 10.1038/srep28781

34. Colson P, Rolain JM, Lagier JC, Brouqui P, Raoult D. Chloroquine and hydroxychloroquine as available weapons to fight COVID-19. Int J Antimicrob Agents 2020; 4:105932. DOI: 10.1016/j.ijantimicag.2020.105932

35. Ponticelli C, Moroni G. Hydroxychloroquine in systemic lupus erythematosus (SLE). Expert Opin Drug Saf 2017;16:411-419. DOI: 10.1080/14740338.2017.1269168

36. Schrezenmeier E, Dörner T. Mechanisms of action of hydroxychloroquine and chloroquine: implications for rheumatology. Nat Rev Rheumatol 2020;16:155-166. DOI: 10.1038/s41584-020-0372-x

37. Zeballos RS1, Fox RI, Cheresh DA, McPherson RA. Anti-glycosphingolipid autoantibodies in rheumatologic disorders. J Clin Lab Anal 1994; 8:378-384. DOI: 10.1002/jcla.1860080607

38. McDonald G, Deepak S, Miguel L, Hall CJ, Isenberg DA, Magee AI, Butters T, Jury EC. Normalizing glycosphingolipids restores function in CD4+ T cells from lupus patients. J Clin Invest 2014;124:712-724. DOI: 10.1172/JCI69571

39. Hammache D, Yahi N, Maresca M, Piéroni G, Fantini J. Human erythrocyte glycosphingolipids as alternative cofactors for human immunodeficiency virus type 1 (HIV-1) entry: evidence for CD4-induced interactions between HIV-1 gp120 and reconstituted membrane microdomains of glycosphingolipids (Gb3 and GM3). J Virol. 1999;73:5244-8. PMID: 10233996

40. Neu U, Woellner K, Gauglitz G, Stehle T. Structural basis of GM1 ganglioside recognition by simian virus 40. Proc Natl Acad Sci USA 2008; 105:5219-24. DOI: 10.1073/pnas.0710301105.

Figure legends

Figure 1. Structures of azithromycin (ATM) and SARS-CoV-2 spike protein trimer.

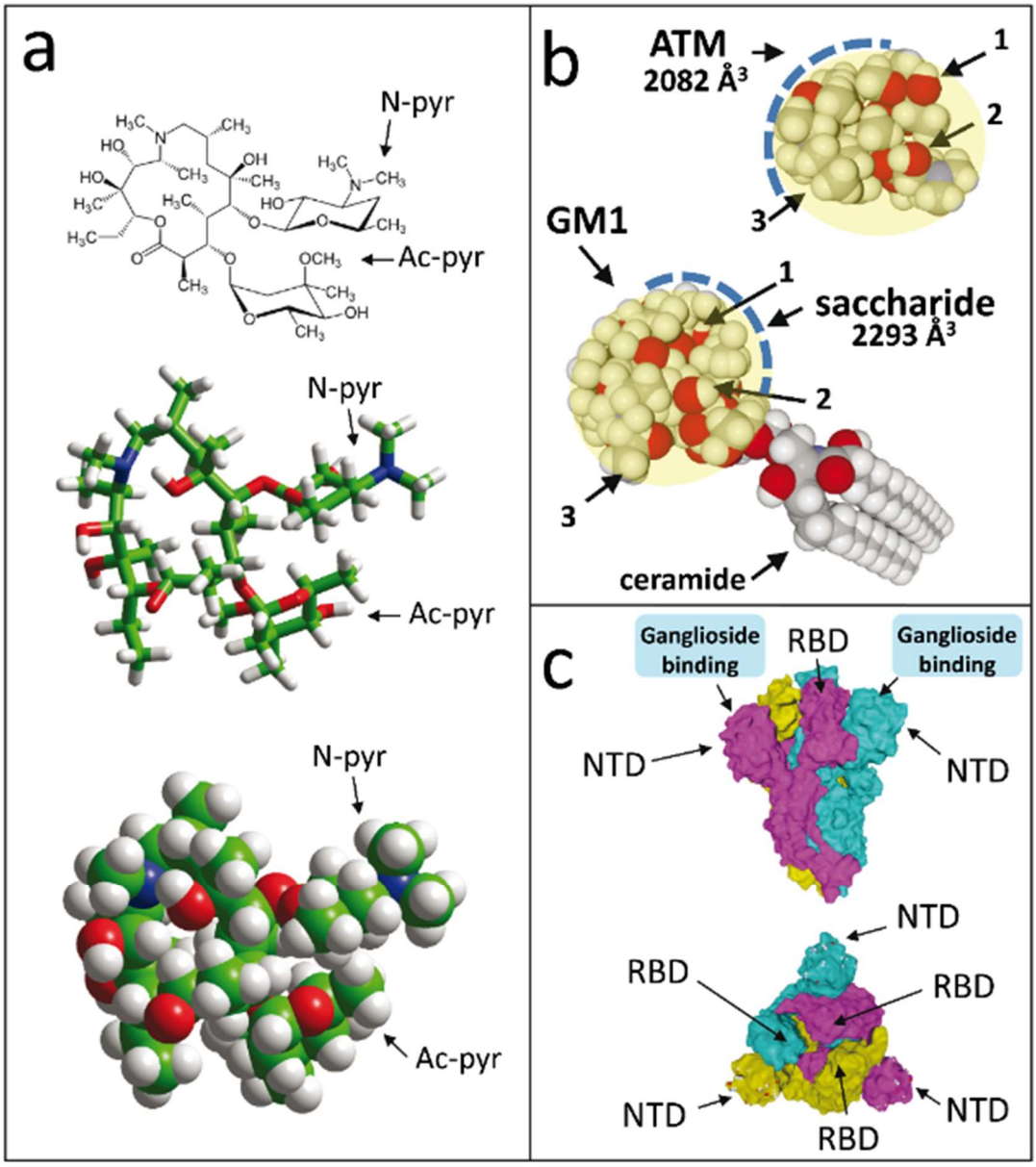

(**a**) ATM, with both sugar-like pyranyl groups N-pyr and Ac-pyr indicated. The molecules are shown in chemical, tube and sphere rendering (carbon green, nitrogen blue, oxygen red, hydrogen white). (**b**) Molecular structure similarity between ATM and the saccharide part of ganglioside GM1. Both structures can adopt a globular shape whose surface is covered with a patchwork of OH (arrows 1 and 2) and CH groups (arrow 3). The volume occupied by ATM and the saccharide part of GM1 can be estimated to 2082 and 2293 $Å^3$, respectively. (**c**) front and above views of the trimeric spike, each spike protein subunit with a distinct surface color (cyan for chain A, yellow for chain B, purple for chain C). Atoms belonging to the ganglioside-binding domain of each subunit are visible underneath the slightly transparent surface. The ganglioside-binding domains, the NTD and the RBD are indicated.

Figure 2. Molecular complex between the SARS-CoV-2 spike protein trimer and ATM.

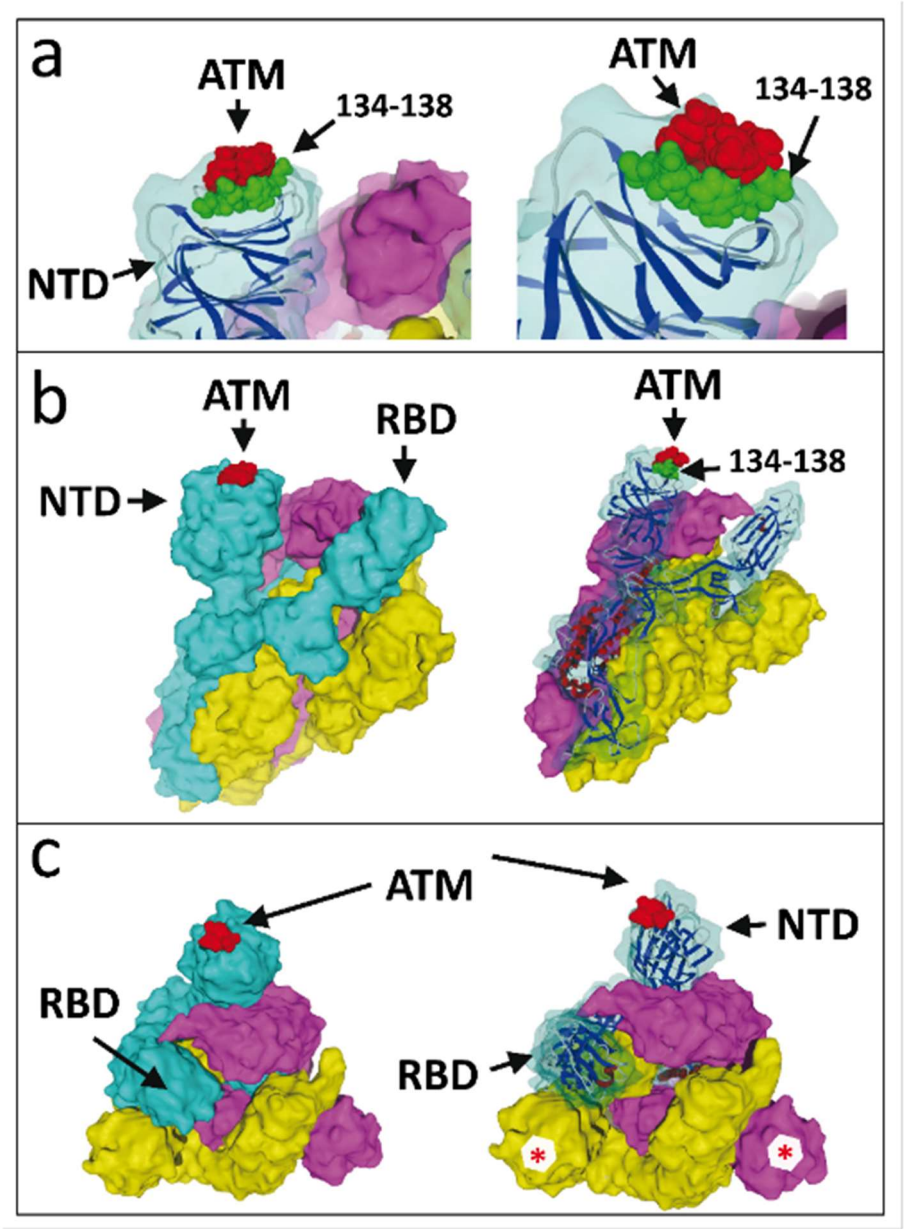

(**a**) Detailed view of ATM bound to the NTD tip of SARS-CoV-2 spike protein chain A, shown at two distinct magnifications and orientations (left and right panels). Note that the NTD tip displays a complementary landing surface for ATM (highlighted in red). The protein stretch 134-138, which contains the QFN triad, is highlighted in green. (**b**) The trimeric structure of the SARS-CoV-2 spike is represented in surface rendition with subunit (protein chain A, B and C) in cyan, yellow and purple, respectively. AMT (in red) is bound to the tip of the NTD domain of the A subunit (left panel). The ribbon structure of the cyan (chain A) subunit is shown in the right panel. (**c**) Above views of the spike-ATM complex. Note that the B and C subunits also display a fully accessible ATM binding site (red asterisk).

Figure 3. Induced-fit conformational rearrangements during binding of ATM on the spike protein.

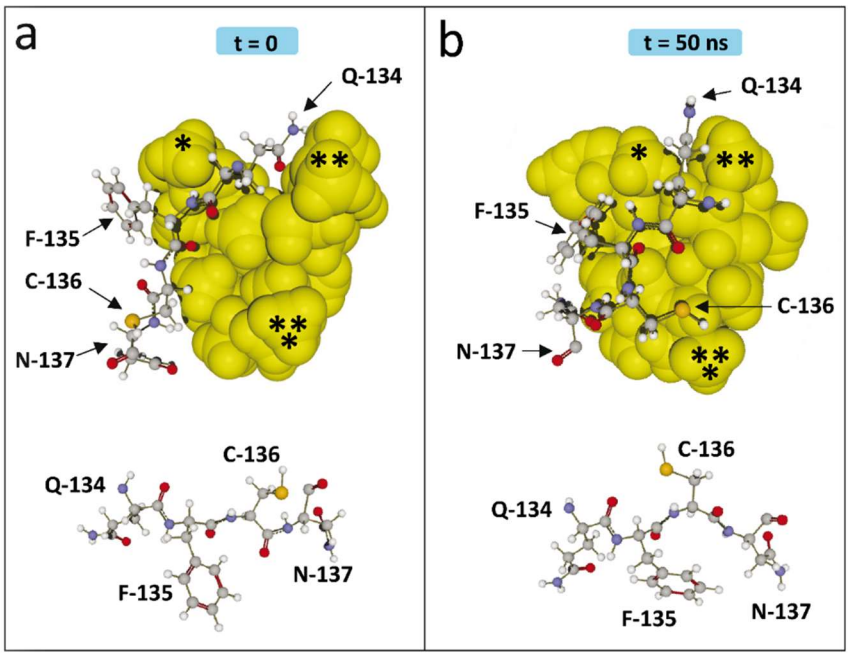

(**a**) Docking of ATM on the spike protein (time = 0). ATM is in yellow spheres, and the protein segment 134-137 is in balls and sticks rendition. Three parts of the ATM molecule are marked with asterisks. The orientation of the side chains of residues 134-137 is shown under the complex. (**b**) ATM bound to the spike protein after MD simulations (time = 50 ns). Note that the complex has evolved according to a typical induced-fit mechanism. The asterisks on ATM help visualizing its conformational changes. Reorientation of amino acid side chains is also clearly visible in the ATM-spike complex and in the isolated 134-137 fragment shown under the complex.

Figure 4. Schematic of ATM interaction at the tip of the spike protein.

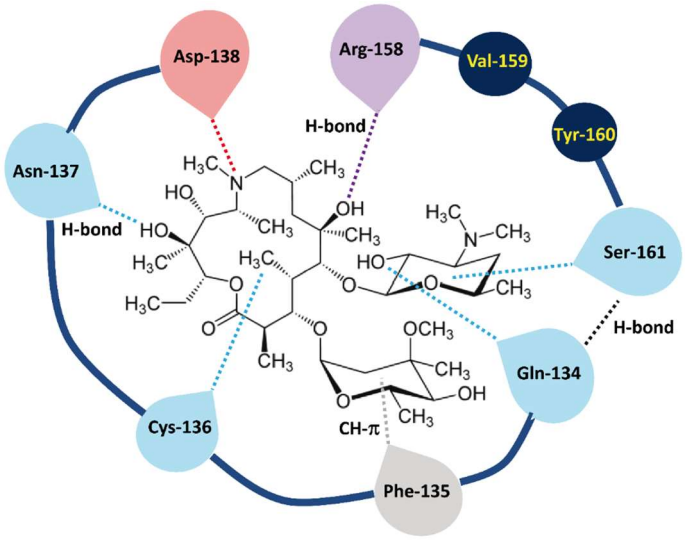

Residues lining cavity under 3.5Å are shown. Hydrogen bonds and CH-π stacking interactions are indicated. Note that Q-134 (Gln-134) and S-161 (Ser-161) are linked by a hydrogen bond which contributes stabilizing the ATM-spike complex.

Figure 5. Energy of interaction of spike protein-ATM and spike-GM1 complexes.

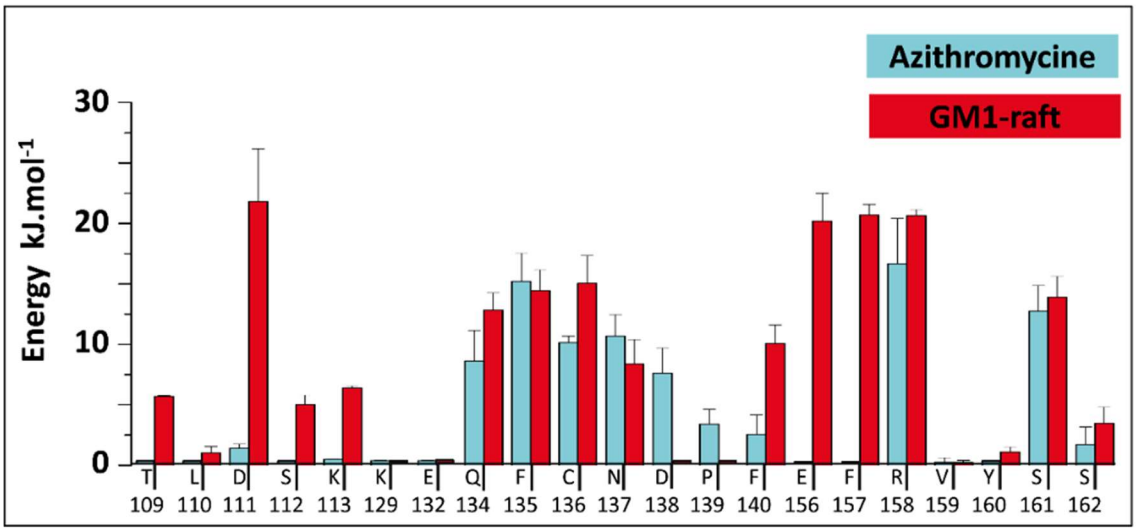

Results are expressed by amino acid residue as mean ± SD of three distinct MD simulations (50 ns) with same starting docking conditions. In the case of GM1, the simulations are done in presence of sphingomyelin and cholesterol to mimic a lipid raft plasma membrane domain. Each bar corresponds to a single amino acid residue, as indicated in the horizontal axis. Detailed values and statistics are shown in Table S1.

Figure 6. MD simulations of GM1-spike protein interaction in a lipid raft domain.

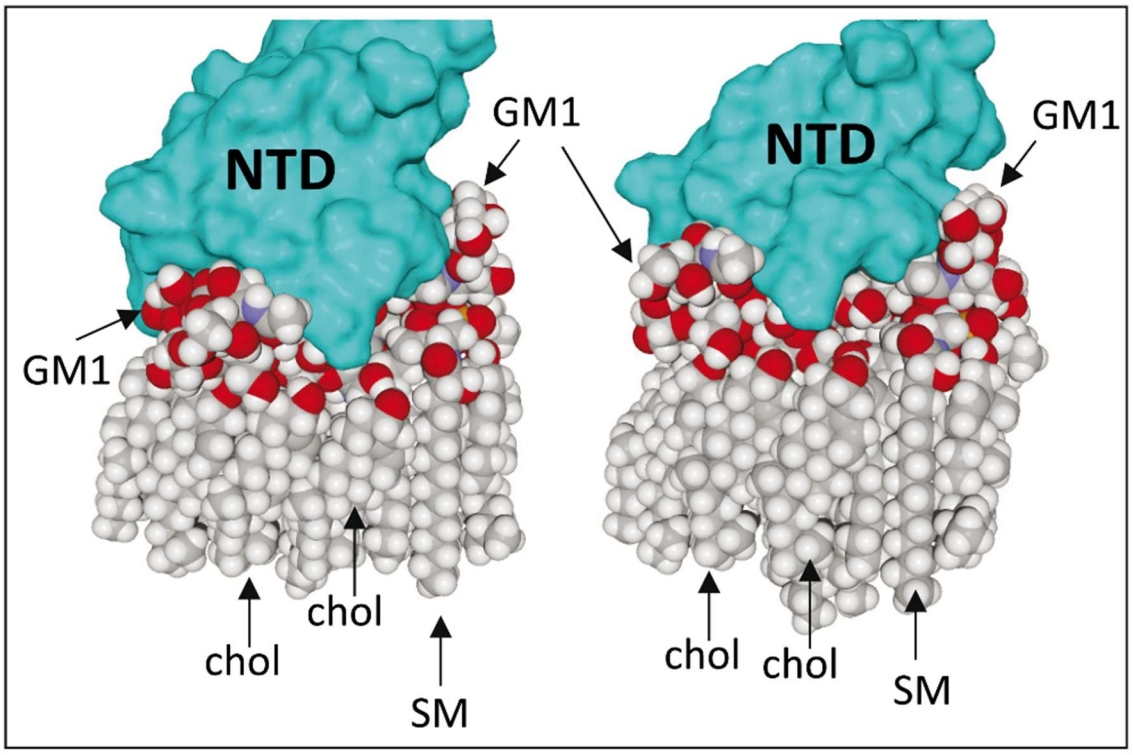

Two GM1 gangliosides were merged with eight cholesterol (chol) and two sphingomyelin (SM) lipids. After initial docking, MD simulations were performed for 50 ns. Two distinct views of the complex are shown. Cholesterol and sphingomyelin stabilize a dimer of GM1 clamped by the NTD of the spike protein.

Figure 7. Amino acid sequence alignments of the ganglioside/ATM binding domain of the SARS-CoV-2 spike protein.

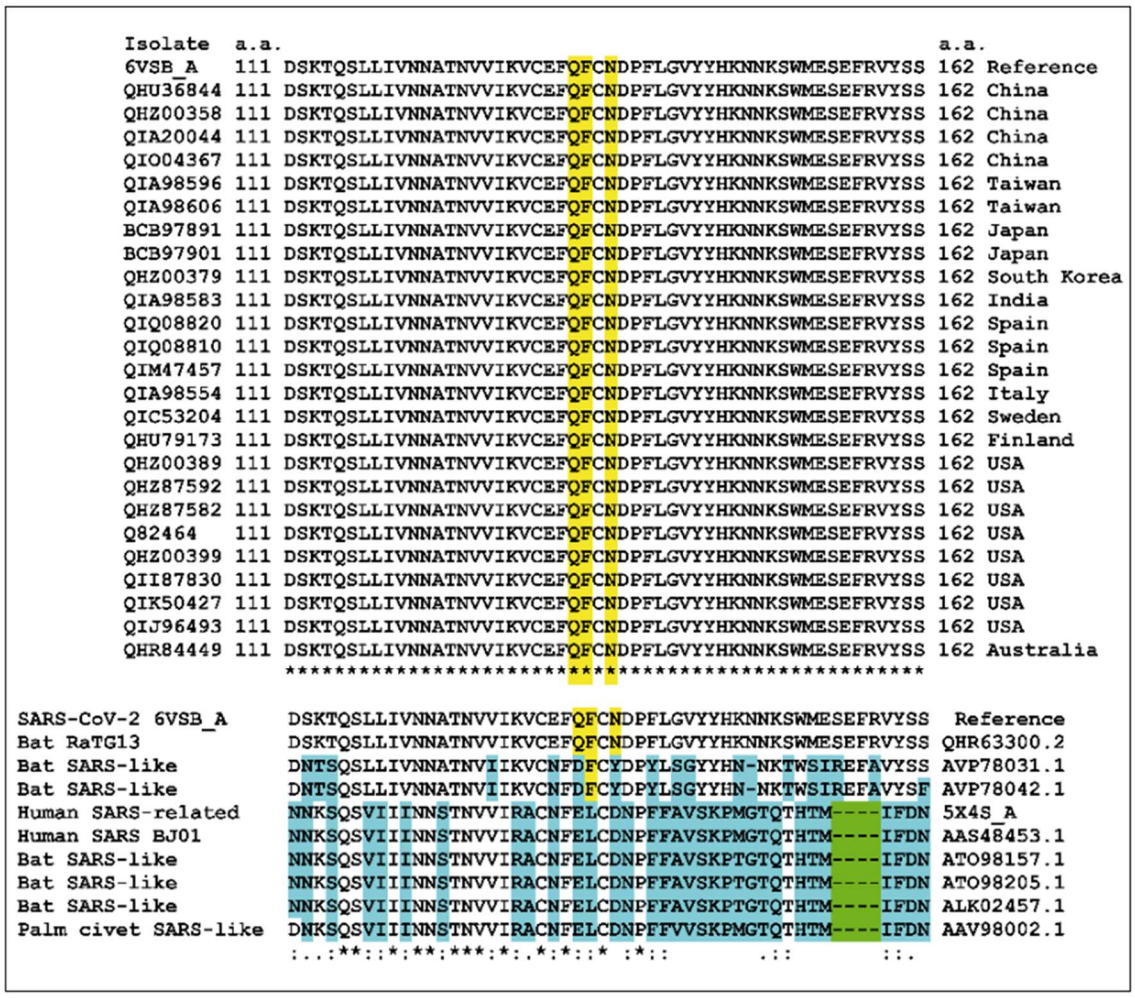

The first group of sequences includes clinical SARS-CoV-2 isolates from various geographic origins aligned with the reference sequence (6VSB_A, fragment 111-162). The QFN triad is highlighted in yellow. The second group of sequences includes human and animal viruses compared with SARS-CoV-2. Deletions are highlighted in green, amino acid changes are highlighted in blue, conserved residues of the QFN triad are highlighted in yellow. The degree of conservation observed in each column is symbolized by an asterisk (*) when the residue is fully conserved, a colon (:) for distinct residues with strongly similar properties (scoring > 0.5 in the Gonnet PAM 250 matrix), and a period (.) for distinct residues with weakly similar properties (scoring ≤ 0.5 in the Gonnet PAM 250 matrix.

Figure 8. CLQ-OH/ATM combination therapy at the molecular level.

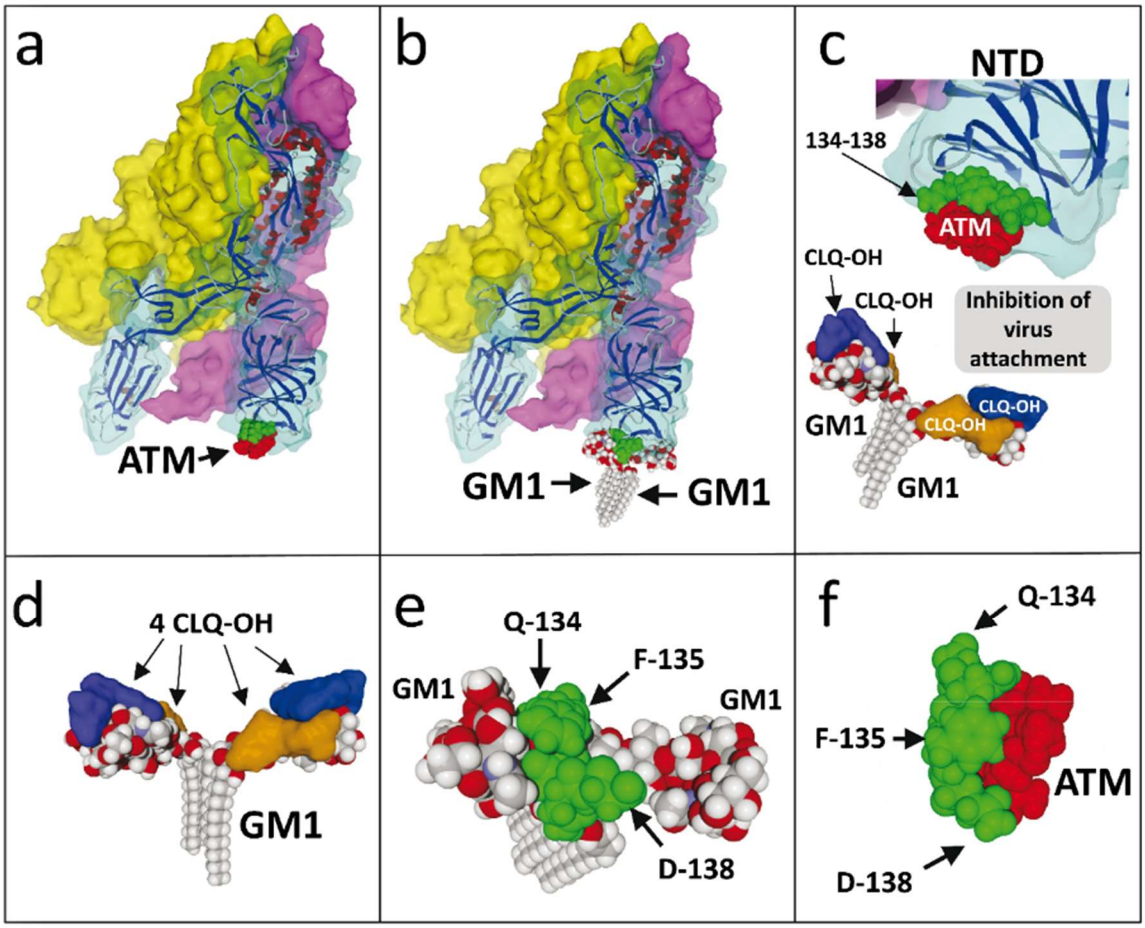

(**a**) ATM bound to the SARS-CoV-2 spike protein trimer. (**b**) Ganglioside dimer (two symmetrically arranged GM1 molecules in a typical chalice-like shape, just like the one evidenced in lipid raft simulations) bound to SARS-CoV-2 spike protein trimer. Note that both ATM and gangliosides share the same binding region. (**c**) AMT prevents ganglioside binding to the SARS-CoV-2 spike protein trimer. CLQ-OH, once bound to gangliosides (blue and orange surfaces), also prevents any interaction with the viral spike (translucid orange disk). (**d**) 4 CLQ-OH molecules bound to a ganglioside dimer. Each GM1 molecule is blocked by two CLQ-OH molecules (blue and orange surfaces) which wrap around the saccharide part. (**e**) Detail of the 134-138 SARS-CoV-2 spike protein stretch bound to GM1. Note that the ganglioside interacts with Q-134 and F-135, but not with D-138. (**f**) Detail of the 134-138 SARS-CoV-2 spike protein stretch bound to ATM. In this case, the binding site includes D-138 in addition to Q-134 and F-135. Note that N-137, which interacts with both ATM and GM1, is not visible in these representations since it is located behind.

Synergistic antiviral effect of hydroxychloroquine and azithromycin in combination against SARS-CoV-2 : what molecular dynamics studies of virus-host interactions reveal

Jacques Fantini, Henri Chahinian and Nouara Yahi

Supporting Figures

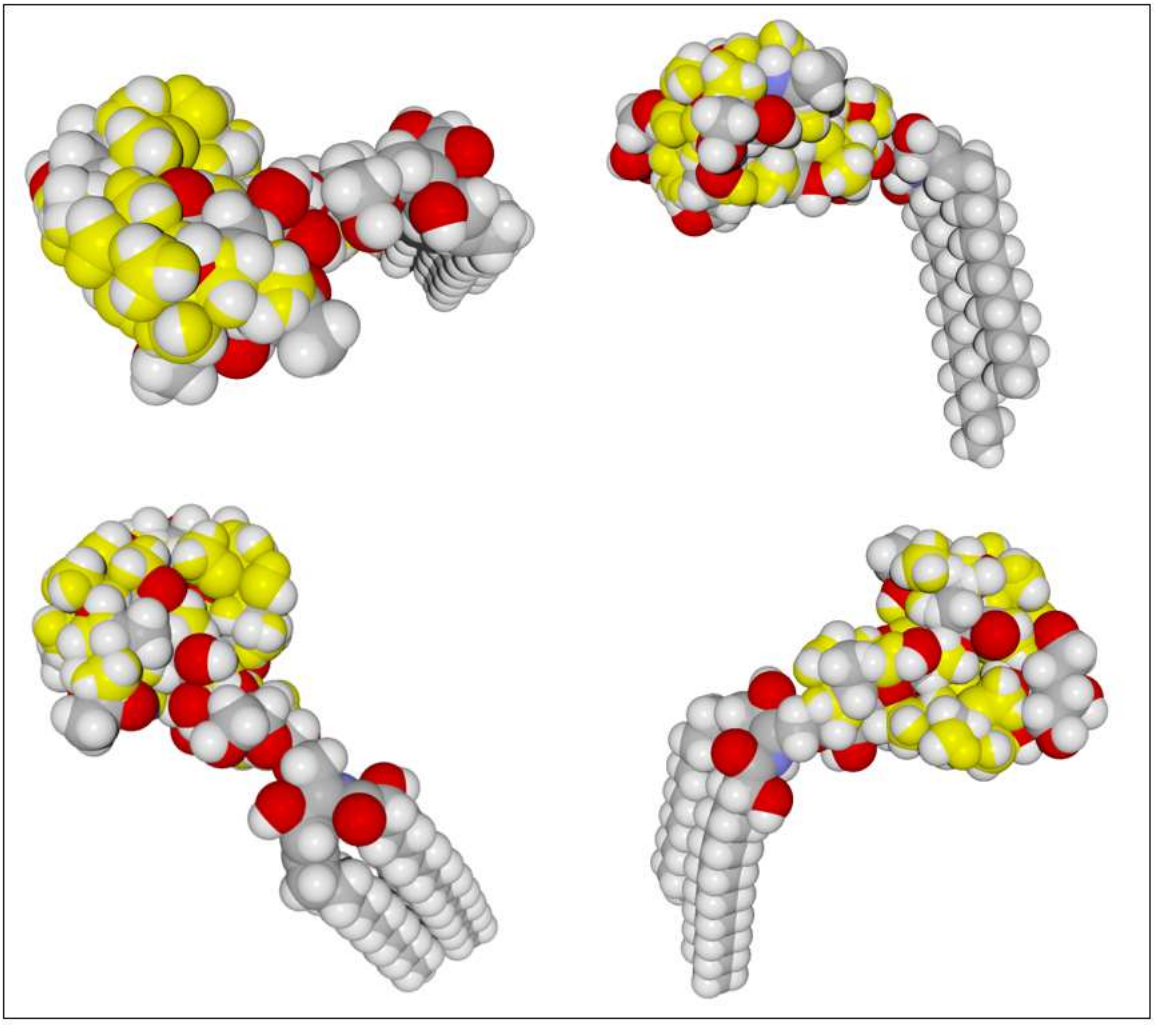

Figure S1. Superposition of azithromycin (in yellow) on the saccharide part of ganglioside GM1 (Hydrogen atoms in white, carbon in grey, oxygen in red and nitrogen in blue). Four different views of the superposed molecules are presented.

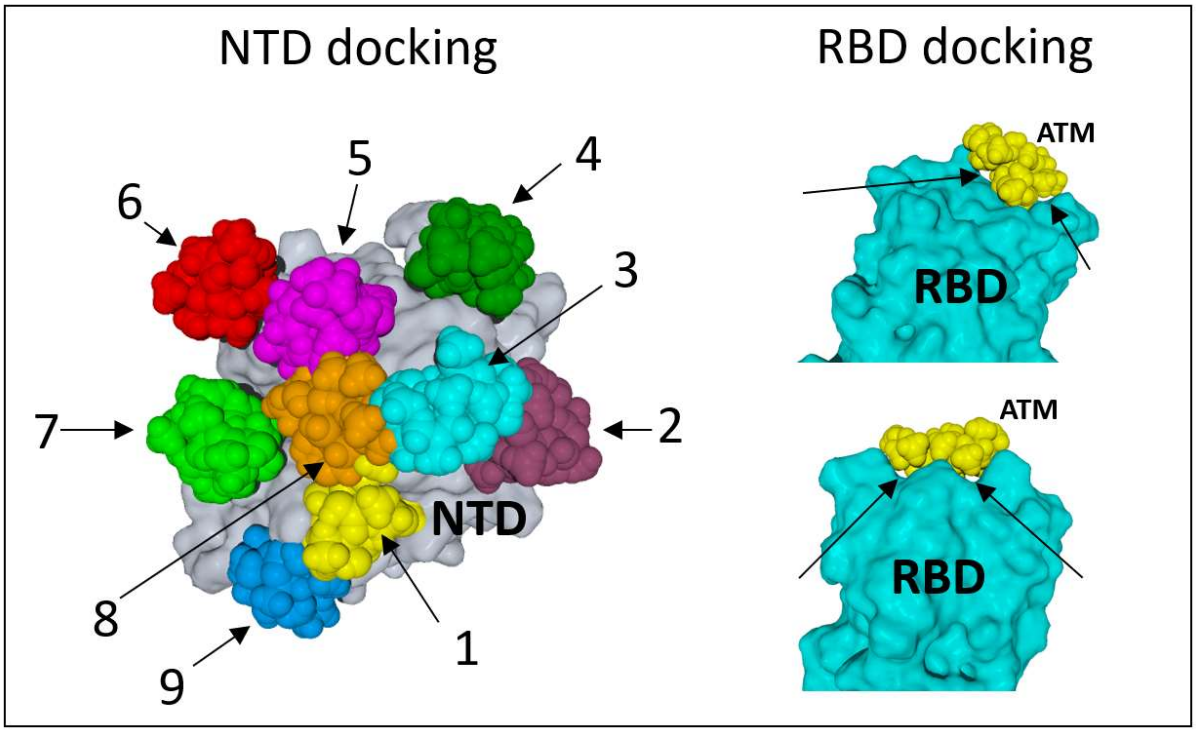

Figure S2. Initial conditions for the docking of azithromycin (ATM) on SARS-CoV-2 spike protein. Left panel: representative examples of docking attempts of ATM molecules on the N-terminal domain (NTD) of the spike protein (in grey). ATM molecules are numbered from 1 to 9, each with a distinct colour. ATM #1 (yellow) is the one for which a stabilized complex could be obtained through MD simulations (described in Figures 3 and 4 of the article). Right panels: unsuccessful docking assays of ATM (in yellow) on the tip of the receptor-binding domain (RBD) of the spike protein (in blue). Note the gaps between ATM and the spike surface (arrows) that explain why these complexes aborted.

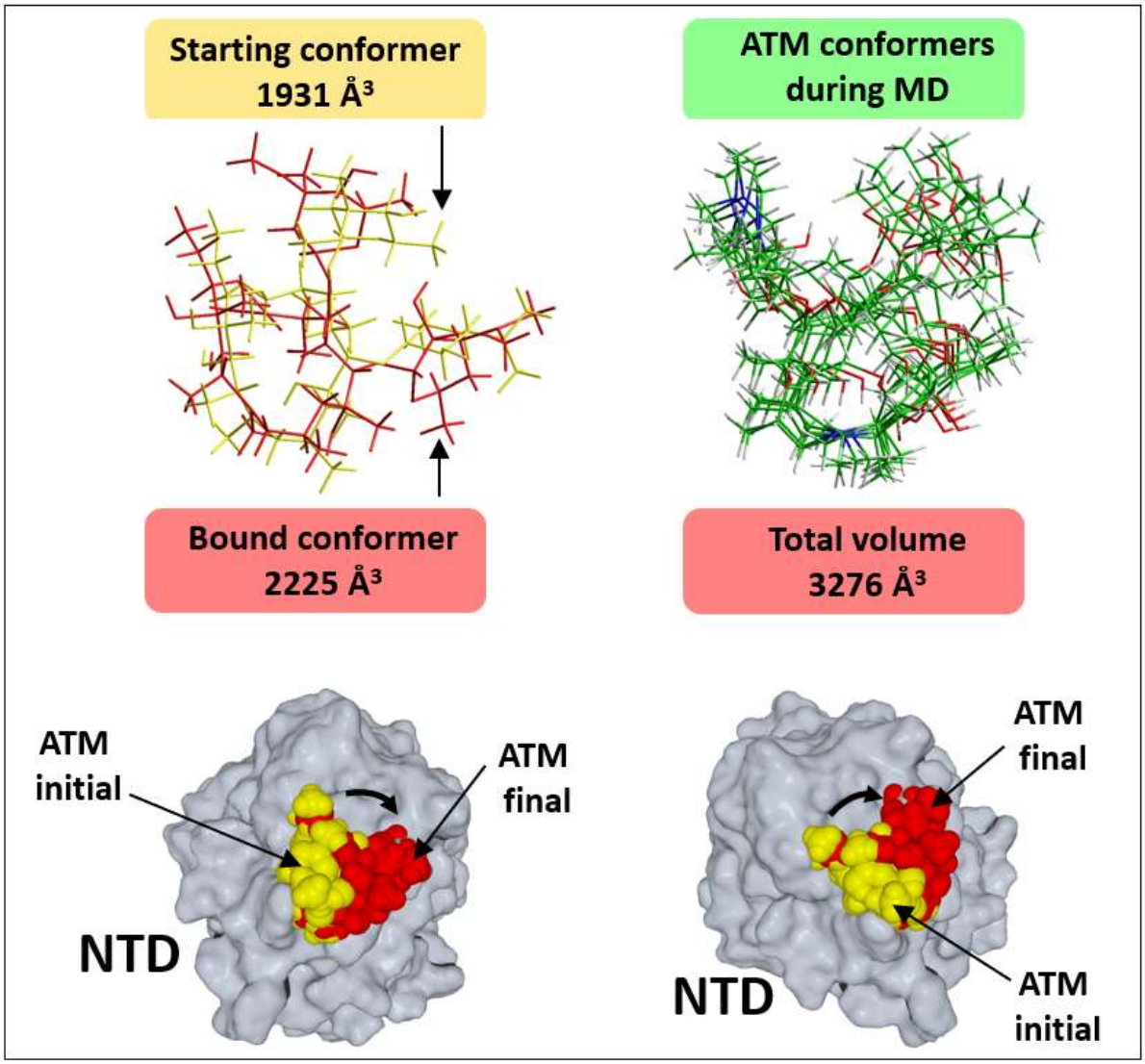

Figure S3. Azithromycin (ATM) trajectories during MD simulations. Upper left: superposition of the initial conformer obtained after docking (tube rendering in yellow) and the final bound conformer obtained after MD simulations (in red). The volume occupied by each of these ATM conformers is indicated (as calculated by the quantitative structure-activity relationship QSAR function of the Hyperchem program, Hypercube, Inc., 1115 NW 4th Street, Gainesville, Florida 32601, USA). Upper right: superposition of ATM conformers obtained during MD simulations. The whole volume occupied by the superposition of these conformers is indicated. Lower panels: two distinct views of the N-terminal domain (NTD) of the spike protein in complex with ATM. Docked ATM is in yellow, stable-bound ATM after MD simulations is in red. Note the 45° rotation of ATM position (arrow) during the simulated binding process.

Supporting Table

Table S1. Statistics of MD simulations.

MD simulations were performed in triplicate (MD1, MD2, MD3). In each case, the energy of interaction of individual amino acid residues of the SARS-CoV-2 spike protein and the total energy of interaction (all amino acid contacts) are shown. After each triplicate, the fourth column indicates the mean ± SD. ATM, azithromycin bound to the NTD of the spike protein; GM1, dimer of ganglioside GM1 bound to NTD of the spike protein; GM1-raft, GM1 dimer in a simulated lipid raft membrane domain consisting of two GM1, two sphingomyelin and 8 cholesterol molecules. The energy of interaction was determined with the Ligand Energy Inspector of the Molegro program (Thomsen R, Christensen MHMolDock: A New Technique for High-Accuracy Molecular Docking. J Med Chem 2006; 49: 3315-21. http://dx.doi.org/10.1021/jm051197e). Amino acid residues 134-137, which contain the QFN triad, are highlighted in blue. Other key residues involved in ATM binding are highlighted in grey.

Spike protein amino acid	*Energy of interaction (in kJ.mol^{-1})*											
	ATM MD1	**ATM MD2**	**ATM MD3**	**ATM mean ± SD**	**GM1 MD1**	**GM1 MD2**	**GM1 MD3**	**GM1 mean ± SD**	**GM1-raft MD1**	**GM1-raft MD2**	**GM1-raft MD3**	**GM1-raft mean ± SD**
Thr-109	0	0	0	**0**	- 5.8	- 5.9	- 6.8	**- 6.17 ± 0.45**	- 5.7	- 5.8	- 5.7	**- 5.73 ± 0.05**
Leu-110	0	0	0	**0**	- 1.6	- 1.2	- 1.3	**- 1.37 ± 0.17**	- 1.1	- 1.6	- 0.3	**- 1.00 ± 0.54**
Asp-111	- 1.9	- 1.2	- 1.1	**- 1.40 ± 0.36**	- 26.1	- 25.6	- 25.6	**- 25.77 ± 0.24**	- 23.1	- 26.4	- 15.9	**- 21.80 ± 4.38**
Ser-112	0	0	0	**0**	- 6.5	- 6.9	- 8.3	**- 7.23 ± 0.77**	- 4.5	- 6.1	- 4.3	**- 5.00 ± 0.81**
Lys-113	- 0.5	- 0.5	- 0.4	**- 0.47 ± 0.05**	- 7.9	- 5.9	- 5.4	**- 6.40 ± 1.08**	- 6.6	- 6.4	- 6.2	**- 6.40 ± 0.16**
Lys-129	- 0.4	- 0.3	- 0.4	**- 0.37 ± 0.04**	0	0	0	**0**	0	0	0	**0**
Glu-132	- 0.4	- 0.4	- 0.3	**- 0.37 ± 0.04**	0	0	0	**0**	0	0	0	**0**
Gln-134	- 12.2	- 6.8	- 6.9	**- 8.63 ± 2.52**	- 14.3	- 11.9	- 14.1	**- 13.43 ± 1.09**	- 11.1	- 14.6	- 12.8	**- 12.84 ± 1.42**
Phe-135	- 17.6	- 16.0	- 12.0	**- 15.20 ± 2.35**	- 11.8	- 12.1	- 12.8	**- 12.23 ± 0.42**	- 15.4	- 12.0	- 15.9	**- 14.43 ± 1.73**
Cys-136	- 9.9	- 10.9	- 9.6	**- 10.13 ± 0.55**	- 18.3	- 17.2	- 15.7	**- 17.07 ± 1.07**	- 13.5	- 18.3	- 13.3	**- 15.03 ± 2.31**
Asn-137	- 12.1	- 11.8	- 8.2	**- 10.70 ± 1.77**	- 11.7	- 11.5	- 6.9	**- 10.03 ± 2.22**	- 8.5	- 10.8	- 5.9	**- 8.40 ± 2.00**
Asp-138	- 4.7	- 9.3	- 8.9	**- 7.63 ± 2.08**	0	0	0	**0**	0	0	0	**0**
Pro-139	- 1.8	- 4.6	- 3.9	**- 3.43 ± 1.19**	0	0	0	**0**	0	0	0	**0**
Phe-140	- 0.3	- 4.2	- 3.1	**- 2.53 ± 1.64**	- 8.0	- 8.1	- 8.0	**- 8.03 ± 0.05**	- 11.5	- 8.0	- 10.8	**- 10.10 ± 1.51**
Glu-156	0	0	0	**0**	- 25.6	- 21.3	- 23.1	**- 23.33 ± 1.76**	- 19.8	- 23.2	- 17.6	**- 20.20 ± 2.30**
Phe-157	0	0	0	**0**	- 21.2	- 20.9	- 22.6	**- 21.57 ± 0.74**	- 19.5	- 21.0	- 21.6	**- 20.70 ± 0.88**
Arg-158	- 11.8	- 20.9	- 17.3	**- 16.67 ± 3.74**	- 21.5	- 22.1	- 19.9	**- 21.17 ± 0.93**	- 19.1	- 20.9	- 21.1	**- 20.63 ± 0.52**
Val-159	0	0	- 0.8	**- 0.27 ± 0.38**	- 0.3	0	0	**- 0.10 ± 0.14**	- 0.3	- 0.4	0	**- 0.23 ± 0.17**
Tyr-160	0	0	- 0.4	**- 0.13 ± 0.19**	- 1.2	- 0.9	- 1.5	**- 1.20 ± 0.24**	- 1.1	- 1.6	- 0.6	**- 1.10 ± 0.41**
Ser-161	- 14.9	- 13.5	- 9.8	**- 12.73 ± 2.15**	- 15.9	- 14.8	- 14.7	**- 15.13 ± 0.54**	- 14.7	- 15.5	- 11.5	**- 13.90 ± 1.73**
Ser-162	- 1.7	0	- 3.5	**- 1.73 ± 1.42**	- 4.9	- 4.9	- 4.9	**- 4.90 ± 0.00**	- 3.5	- 5.1	- 1.8	**- 3.47 ± 1.35**
Total	**- 90.2**	**- 100.4**	**- 86.6**	**- 92.40 ± 5.84**	**-202.6**	**- 191.2**	**- 191.1**	**- 195.00 ± 5.40**	**- 179.0**	**- 197.7**	**- 165.3**	**- 180.67 ± 13.28**